Small

NANO · MICRO small
www.small-journal.com

RESEARCH ARTICLE

Anti-Swelling and Thermally-Actuated Adhesive Dual-Network Hydrogel for Annulus Fibrosus Repair With Self-Healing Capability

Qiangwang Geng[1] | Haoran Zhang[2,3] | Tao Guo[1] | Yiwei Zhao[2] | Jianguo Zhang[2] | Fenghua Zhang[1] | Shengru Wang[2] | Jinsong Leng[1]

[1]Centre for Composite Materials and Structures, Harbin Institute of Technology (HIT), Harbin, People's Republic of China | [2]Department of Orthopedic Surgery, Peking Union Medical College Hospital, Peking Union Medical College and Chinese Academy of Medical Sciences, Beijing, China | [3]Department of Spinal Surgery, Peking University People's Hospital, Peking University, Beijing, China

Correspondence: Fenghua Zhang (fhzhang_hit@163.com) | Shengru Wang (wangshengru@foxmail.com) | Jinsong Leng (lengjs@hit.edu.cn)

Received: 21 April 2026 | **Revised:** 30 June 2026 | **Accepted:** 18 July 2026

Keywords: adhesive hydrogel | annulus fibrosus | anti-swelling | self-healing

ABSTRACT

To prevent nucleus pulposus reherniation following annulus fibrosus (AF) rupture, effective defect sealing is imperative post-discectomy. Ideal repair materials require excellent cytocompatibility, tailored adhesion, and long-term stability. Herein, a double-network hydrogel (PNG) featuring a dense hydrogen-bonded network is engineered by integrating gelatin with poly(acrylic acid-co-N-acryloyl glycinamide) via a pH-controllable crosslinking strategy. PNG exhibits exceptional dimensional stability (swelling ratio <1%) and temperature-responsive adhesion. Molecular dynamics simulations elucidate the adhesion-swelling equilibrium, identifying acrylic acid as the optimal comonomer for robust hydrogen-bonding. The hydrogel demonstrates a smart adhesive transition, achieving robust bonding strength of 274.4 kPa at physiological temperature (40°C), significantly superior to its state at room temperature (152.6 kPa), thus facilitating intraoperative handling. This provides robust interfacial adhesion sufficient to secure the defect site and withstand physiological conditions, ensuring reliable tissue-material integration. In a rat AF defect model, PNG effectively seals the defect, restores mechanical integrity, and promotes the regeneration of extracellular matrix components (COL1, COL2, and ACAN). This multifunctional hydrogel achieves a delicate adhesion-swelling balance, providing a novel biomimetic scaffold strategy to prevent postoperative reherniation and guide functional tissue regeneration.

1 | Introduction

Lumbar disc herniation (LDH) is a major disabling condition caused by herniation of the nucleus pulposus (NP) through a ruptured annulus fibrosus (AF) and subsequent nerve compression [1–4]. Although minimally invasive procedures, such as percutaneous endoscopic lumbar discectomy (PELD), are the standard of care, the inherent avascularity of intervertebral discs severely limits their self-repair capacity. Consequently, postoperative annular defects pose significant challenges, often leading to reherniation and degenerative collapse [5–9]. Although clinical suturing techniques exist, they are technically demanding, costly, and frequently fail to restore mechanical integrity [10–12]. Various biomaterials have been developed to enhance AF repair [13–15]. Among these, hydrogel-based bioadhesives have emerged as promising candidates for AF repair because of

Qiangwang Geng and Haoran Zhang contributed equally as the first author.

their biocompatibility and similarity to the natural extracellular matrix (ECM) [16–20]. However, current hydrogel systems are plagued by an intrinsic dilemma: the antagonistic relationship between mechanical stability (requiring dense crosslinking) and tissue adhesion (requiring dynamic chain mobility). This trade off often leads to either weak bonding or excessive swelling in vivo. Most of the existing formulations suffer from complex handling, insufficient strength, weak tissue adhesion, or excessive swelling [21–25]. Crucially, in vivo swelling can exert detrimental radial pressure on the AF, thus exacerbating tissue tearing and compromising the adhesive interface, ultimately causing repair failure [26–30]. Although hydrophobic interactions can mitigate swelling, they invariably suppress interfacial adhesion [31]. Therefore, the development of a bioadhesive that simultaneously achieves robust adhesion, anti-swelling stability, and self-healing capability remains an urgent need for AF repair.

Addressing the specific requirements of AF repair requires reconciling the mismatch between rigid mechanical stability and dynamic adaptability [32–35]. Achieving high-strength and anti-swelling properties typically requires a dense, stable crosslinked network, which inherently restricts the dynamic chain mobility required for self-healing and wet-tissue adhesion [36–39]. Conversely, networks relying solely on dynamic bonds often lack long-term dimensional stability under physiological loading [40–42]. To resolve this paradox, the rational selection of functional comonomers is crucial. We established a molecular library comprising seven representative hydrophilic monomers and conducted systematic GROMACS MD simulations to evaluate their interaction affinities with the matrix. Guided by the theoretical insights, we designed a dual-network hydrogel inspired by dynamic biological interactions. The first network comprises a copolymer of AAc and N-acryloylglycinamide (NAGA). Here, NAGA provides abundant sites for strong hydrogen bonding, whereas AAc acts as a pH regulator to modulate the interaction strength. This framework is interpenetrated by gelatin, which serves as a dynamic anchor. The reversible conformational change of the gelatin triple helix acts as a thermal switch for stiffness modulation, enhancing wettability and adhesion at physiological temperatures. We propose a mechanism based on a pH-modulated hydrogen-bond crosslinking density threshold, in which a weakly acidic environment drives the transition from electrostatic repulsion to attraction between gelatin and poly(acrylic acid) chains, thus facilitating a robust sol-gel transition.

Herein, we report a multifunctional PNG (PAAc-NAGA-gelatin) hydrogel that integrates anti-swelling, temperature-controlled adhesion, and self-healing functions into a single system. The hydrogel exhibits exceptional dimensional stability (swelling ratio of <1%). By leveraging pH-modulated electrostatic interactions and synergistic hydrogen bonding, the adhesive strength peaks at 274 kPa near body temperature (40°C), enabling easy handling and strong adhesion. Furthermore, the dynamic physical crosslinks within the network endow the material with efficient self-healing capabilities to restore integrity post-damage. In a rat model of AF defects, the PNG hydrogel not only sealed the defect but also significantly upregulated key ECM proteins (COL1, COL2, and ACAN), guiding functional tissue regeneration. By successfully balancing conflicting material properties, this strategy offers a robust solution for intervertebral disc repair and provides a versatile blueprint for the design of tissue-engineering hydrogels.

2 | Results and Discussion

2.1 | Preparation of PNG Hydrogel

Guided by MD simulations and the precise modulation of the dynamic interactions within a highly crosslinked network, we developed a high-performance hydrogel that integrates thermoresponsive adhesion, anti-swelling stability, and self-healing capabilities (Figure 1a). The hydrogel consists of a primary AAc and NAGA network (Figure 1b) that forms a rigid framework via dense hydrogen bonding (Figure 1b(i)). Simultaneously, an interpenetrating gelatin network is introduced. As elucidated by our simulations, a high AAc concentration triggers a pH-modulated transition from repulsion to attraction, enabling gelatin segments to interact with poly(acrylic acid) chains through hydrogen bonds (Figure 1b(ii)) and electrostatic attraction between protonated amino groups (—NH_3^+) and carboxylate anions (—COO^-) (Figure 1b(iii)), stabilizing the interpenetrating network structure. This highly crosslinked architecture effectively restricts polymer chain mobility and inhibits water penetration, endowing the PNG hydrogel with exceptional anti-swelling properties. Consequently, the hydrogel maintains its structural integrity and dimensional stability in the physiological environment. Concurrently, the network exhibits temperature-responsive adhesion; lower adhesion at 20°C facilitates intraoperative handling, whereas strength increases at 40°C to secure tissue fixation. Furthermore, the abundance of dynamic hydrogen bonds confers efficient self-healing properties, enabling the recovery of mechanical integrity after damage via local bond reorganization and functional group reassociation. Therefore, by rationally engineering dynamic noncovalent interactions within a dense framework guided by theoretical predictions, we hypothesize that this PNG hydrogel can achieve synergistic anti-swelling, controllable adhesion, and self-healing functions, making it an ideal candidate for AF repair (Figure 1c).

2.2 | Gelation Mechanism and Molecular Dynamics

To construct a tough and dynamic non-covalent crosslinked network in the hydrogel system, the rational selection of functional comonomers is crucial. To this end, we established a molecular library containing seven representative hydrophilic monomers: acrylamide (AAm), hydroxyethyl acrylate (HEA), hydroxyethyl methacrylate (HEMA), N-isopropylacrylamide (NIPAM), carboxybetaine methacrylate (CBMA), N-methylol acrylamide (NMA), and AAc. They cover the most widely applied classical hydrogen-bonding groups in advanced functional hydrogels (including primary/secondary amide groups, hydroxyl groups, carboxyl groups, and zwitterionic groups). We first used GROMACS MD simulations to systematically screen the comonomers. All MD simulations were performed using GROMACS 2025.3. The gelatin was described using the AMBER ff14SB force field, which is well-validated for reproducing structural dynamics. The polymer monomers (such as AAc, NAGA, and other screened comonomers) were generated

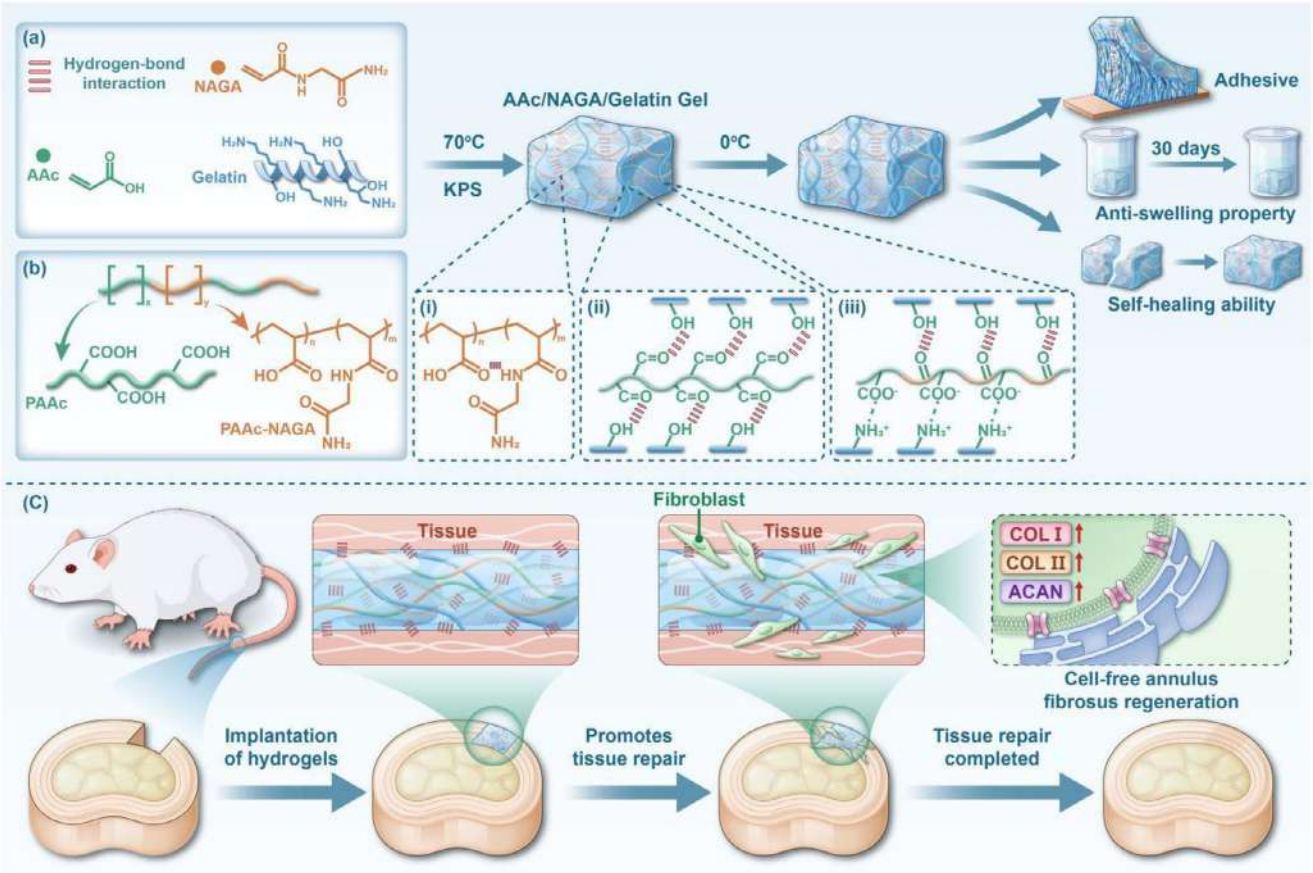

FIGURE 1 | Synthesis mechanism of PNG hydrogel. a) Schematic illustration of the synthesis process of PNG hydrogel along with its adhesion, anti-swelling, and self-healing properties. b) Reaction equation of AAc and NAGA, along with the types of hydrogen bonds: i) Hydrogen bonds between PAAc and PNAGA; ii) Hydrogen bonds between PAAc and gelatin; iii) Electrostatic interactions between PAAc and gelatin. c) Schematic diagram and repair mechanism of PNG hydrogel for AF repair in a rat intervertebral disc model.

using the Generalized Amber Force Field 2 (GAFF2) via Antechamber and ACPYPE, ensuring native compatibility and consistent non-bonded treatment with the protein force field. The aqueous solvent was modeled using the standard TIP3P water model, which avoids artifacts arising from force field-solvent incompatibilities and reliably simulates bulk water properties. The initial configuration of the simulated system is shown in Figure 2a, aiming to systematically evaluate the interaction affinities between these different hydrogen-bonding motifs and the NAGA-gelatin matrix, thereby screening out the optimal comonomer for constructing a highly stable supramolecular network. To provide a comprehensive baseline for this screening, the detailed hydrogen-bonding behaviors of the other six representative monomers interacting with the hydrogel matrix were systematically analyzed showed in Figures S1–S6.

Based on the average number of hydrogen bonds (Figure 2b), the number of hydrogen bonds formed between each monomer and the system is not significantly different, with AAc at a relatively high level and HEA at the lowest. To further evaluate the stability of hydrogen bonds, we calculated the average lifetime of hydrogen bonds (i.e., the time from formation to breakage). As shown in Figure 2c, the hydrogen bond lifetimes formed by the other six monomers are generally maintained at around 35 ps, while lifetime of hydrogen bonds formed by AAc with the system is significantly longer, reaching approximately 42 ps. This indicates that AAc can form a more durable and stable hydrogen bond network with the system. Furthermore, the average bond angle of hydrogen bonds is also an important indicator of hydrogen bond strength (the closer the angle is to 180°, the stronger the hydrogen bond). As shown in Figure 2d, the average bond angle of other monomers is around 145°, while the hydrogen bond angle formed by AAc with the system can reach as high as 151°. Notably, the average bond lengths of various interactions within the system range from 2.7 to 2.9 Å, indicating that stable hydrogen bonding interactions have formed within the system, both between polymer chains and between the polymer and water molecules. Based on the data on the number of hydrogen bonds, lifetime, and bond angle, we have fully demonstrated that AAc can form the strongest and most stable hydrogen bonds in the system. Therefore, AAc was selected as the ideal monomer for copolymerization with NAGA.

Under the premise of keeping the gelatin and water content constant, we deeply explored the influence of different AAc/NAGA mass ratios (from P3N7 to P9N1) on the topological evolution of the internal hydrogen bond network of the system showed in Figures S7–S13. As shown in Figure 2e, the number of hydrogen bonds between gelatin and water molecules increases monotonically with increasing AAc content; conversely, the number

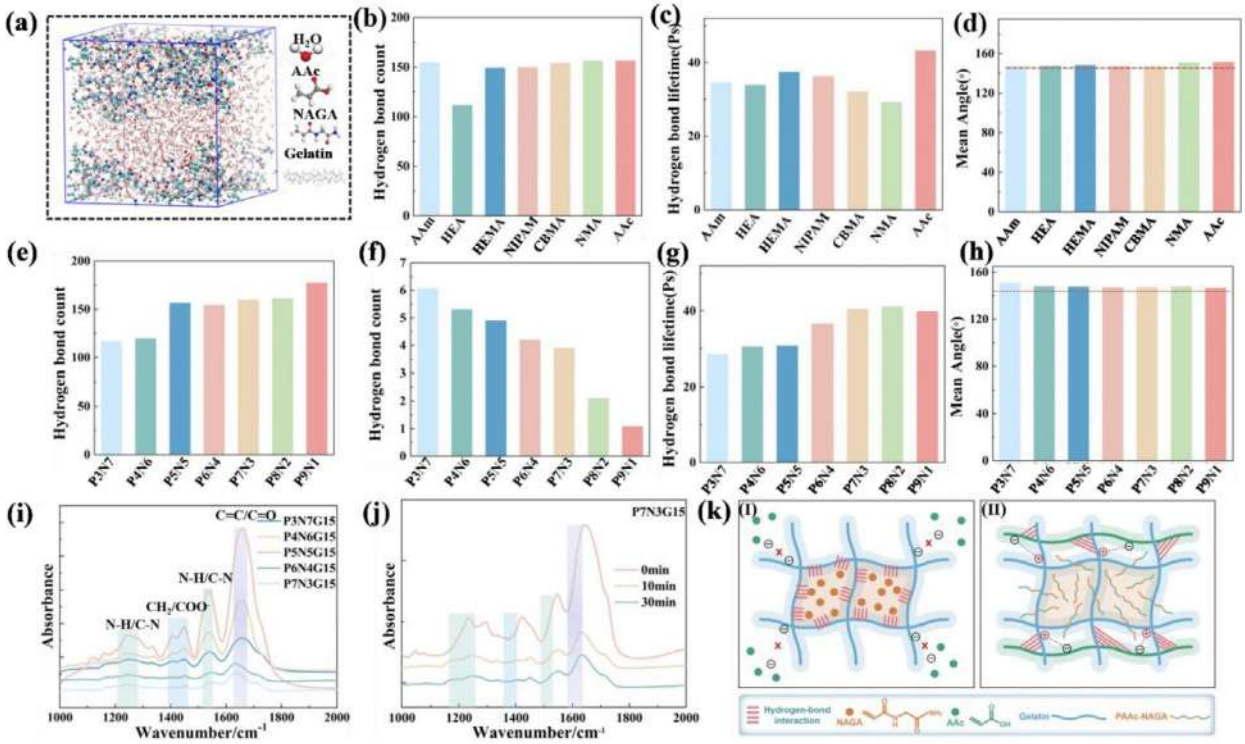

FIGURE 2 | a) GROMACS simulation modeling diagram of the PNG hydrogel system. b) Average number of hydrogen bonds formed between polymer-NAGA and the system. c) Average lifetime of hydrogen bonds formed between polymer-NAGA and the system. d) Bond angle of hydrogen bonds formed between polymer-NAGA and the system. e) Number of hydrogen bonds between gelatin and water at different AAc contents. f) Number of hydrogen bonds between AAc/NAGA and gelatin at different AAc contents. g) Lifetime of hydrogen bonds between AAc and NAGA at different AAc contents. h) Average bond angle of hydrogen bonds formed between AAc/NAGA and gelatin at different AAc contents. i) Infrared spectra of PNG hydrogels with different ratios of AAc and NAGA. j) Infrared spectra of P7N3G hydrogel at different time points. k) Gelation mechanism of the PNG hydrogel.

of hydrogen bonds between the copolymer (PAAc-NAGA) and gelatin gradually decreases (Figure 2f). This phenomenon stems from a pH-driven conformational and interaction transition. At low AAc contents, the binding between the polymer and gelatin mainly depends on the hydrogen bonding between NAGA and gelatin; however, as the AAc content increases and the pH value of the system decreases, the electrostatic repulsion between gelatin and AAc changes to electrostatic attraction. Hydrogen bonds formed between AAc and NAGA significantly enhance both intrachain and interchain interactions within the copolymer, leading to the formation of a dense self-association network. This reduces the number of direct hydrogen bonds between the copolymer and gelatin. More importantly, when the AAc/NAGA ratio exceeds P5N5, the hydrogen bond lifetime between the AAc and NAGA molecular chains is significantly enhanced (Figure 2g). This indicates that high concentrations of AAc trigger strong cooperating hydrogen bonding between and within copolymer chains. This dominant polymer-polymer interaction partially releases gelatin molecules, allowing them to undergo more thorough solvation with water molecules. The slight decrease in the average bond angle of hydrogen bonds between polymers and gelatin with increasing AAc content, as shown in Figure 2h, further confirms this network reconstruction process.

Macroscopic gelation experiments show that a stable hydrogel can only be formed when the AAc/NAGA ratio exceeds the 5:5 threshold (Figure S14i), confirming the conclusion in the MD simulation that hydrogen bond lifetime is enhanced after P5N5. Infrared spectroscopy qualitatively demonstrated the formation of the hydrogen bond network (Figure 2i,j). Combined with macroscopic inverted flask analysis, the hydrogel completed cross-linking and established a solid network; the decrease in absorption intensity of the amide II/III bands (1536, 1243, and 1333 cm^{-1}) directly reflects the deep involvement of amide groups in the construction of a dense hydrogen bond network. Notably, the absence of the carboxylate signal peaks (1406/1448 cm^{-1}) in the spectrum confirms that AAc in the system primarily exists in the protonated -COOH form, thus acting as a potent proton donor in hydrogen bonding.

Theoretical simulations and experimental characterization together establish the core theory of pH-regulated hydrogen bonding density threshold. As illustrated in the mechanism diagram in Figure 2k: at low AAc content (Figure 2k-I), the system pH may be higher than the isoelectric point of gelatin, leading to electrostatic repulsion between components and inhibiting the formation of effective physical cross-linking points; conversely, after exceeding the critical threshold of high AAc content (Figures 2k-II), the decrease in system pH triggers a phase transition from repulsion to attraction, thereby driving the formation of a dense and stable supramolecular network structure dominated by AAc-NAGA and AAc-gelatin synergistic hydrogen bonds. This mechanism is experimentally corroborated

by the pH measurements of the precursor solutions (Figure S15). The pI of the gelatin used in this system is 4.7–5.2, and the pKa of PAAc is approximately 4.5. At low AAc contents (from P3N7 to P4N6), the solution pH decreases from 5.09 to 4.90, which remains near or above the gelatin pI, preventing effective protonation and cross-linking. However, at the critical P5N5 threshold, the pH drops to 4.47 (below the pI). This specifically acidic environment promotes the protonation of gelatin's amino groups ($-NH_3^+$), transforming the electrostatic repulsion into robust attraction with the carboxylate groups (-COO-) of the copolymer, and triggering the macroscopic gelation.

2.3 | Adhesive Behavior of PNG Hydrogels

The adhesive behavior of PNG hydrogels is governed by the synergistic interplay between carboxyl-amide hydrogen bonding and gelatin thermoresponsiveness. To decouple the roles of composition and temperature in adhesion modulation, we systematically compared the PNG hydrogels containing both AAc and NAGA with their NAGA-free counterparts. As shown in Figure 3a, the adhesive strength progressively increased from 71.2 to 152.6 kPa with higher AAc-to-NAGA ratios, whereas NAGA-free hydrogels exhibited diminished adhesion. The corresponding adhesion test curves are presented in Figure S14d–f. This composition-dependent adhesion was correlated with the surface properties through water contact angle measurements, revealing improved wettability (65° for A9N1) with increasing AAc content.

X-ray photoelectron spectroscopy analysis (Figure 3g) revealed distinct chemical shifts, indicating altered electron density distributions around the carboxyl and amide groups. The high-resolution C 1s spectra of the hydrogels were deconvoluted into four distinct components: C—C/C—H at ~284.8 eV, C—O/C—N at ~286.0 eV, C═O at ~288.0 eV, and O—C═O at ~289.0 eV. Notably, as the AAc content increased from P7N3G to P9N1G, there was a visible increase in the relative peak areas of the C═O and O—C═O components (increasing from approximately 16.55% to 20.52%), indicating a significant enrichment of oxygen-containing functionalities. Combined with the FTIR, these data support the presence of hydrogen-bonding interactions in the hydrogel network.

A distinct temperature-dependent adhesive transition was observed (Figure 3b,c). Adhesive strength for the A9N1 formulation peaked at 274.4 kPa at 40°C (near body temperature), which was significantly higher than that at 20°C (152.6 kPa) or 60°C (87.7 kPa). This tunability originates from the structural evolution of gelatin: at 20°C, gelatin maintains a stable triple-helix conformation, and the hydrogel remains relatively rigid (Figure 3h(I)). At 40°C, the helical structure of gelatin unfolds, and the hydrogel transitions into a soft state (Figure 3h(II)), resulting in significant deformation during detachment, where the rupture and reformation of reversible hydrogen bonds dissipate substantial energy. Further heating to 60°C weakens adhesion due to excessive hydrogen bond dissociation, as schematically illustrated in Figure 3h(III). The PNG hydrogel exhibits excellent adhesion properties, highlighting its potential as an effective bioadhesive for clinical intervertebral disc AF repair. The hydrogel's primary function is as a tissue sealant, rather than a complete structural replacement. The achieved interfacial adhesion strength of 274.4 kPa is designed to provide optimal pressure sealing for the defect interface. This adhesion strength is highly competitive clinically among soft tissue bioadhesives because it is sufficient to withstand the physiological extrusion pressure of the nucleus pulposus and maintain defect closure during the critical early stages of tissue regeneration.

To further clarify the thermal responsiveness of the gelatin component, DSC was performed under a nitrogen atmosphere (Figure S16). The DSC curve suggests that gelatin undergoes a thermal transition in the range of 30°C–40°C. This transition region is close to physiological temperature and agrees well with the temperature window in which the hydrogel exhibits enhanced adhesion.

To elucidate the molecular mechanism of this thermal transition, temperature-dependent 2D-IR spectroscopy of P9N1G15 was used to provide molecular-level insights into the hydrogen bonding dynamics (Figure 3f). The conventional temperature-dependent normal IR spectra were showed in Figure S17. The synchronous map displayed three autopeaks at Ψ(1720, 1720), Ψ(1635, 1635), and Ψ(1544, 1544) cm^{-1}, corresponding to non-hydrogen-bonded C═O, hydrogen-bonded amide C═O, and hydrogen-bonded N—H, respectively. The 1720 cm^{-1} reading is attributed to the C═O stretching vibration of the carboxyl group on the AAc unit. Increased temperature leads to the dissociation of the hydrogen bonds between AAc and the amide group, thereby exposing more unbonded free carboxyl groups. The hydrogel contains an extensive hydrogen-bonding network (H···O—H, C═O···H, N—H···O) that progressively dissociates with heating, and the thermally triggered disassembly follows a specific sequence: C═O···H bonds break initially, followed by other interactions, including H···N—H.

To further assess the tissue adhesion performance of the PNG hydrogel, in situ adhesion tests were performed on various substrates (Figure 3d). The P9N1 hydrogel successfully adhered to heart, liver, and kidney tissues. Overall, our findings suggest that the P9N1 PNG hydrogel demonstrates superior adhesive performance, highlighting its potential as an effective bio-adhesive for clinical AF repair. Notably, the hydrogel exhibited significant underwater adhesion, with the strength increasing from 30.8 to 60 kPa (Figure 3e; Figure S14g), highlighting its applicability in fluid-rich surgical environments.

2.4 | Mechanical, Self-Healing, and Anti-Swelling Properties of PNG Hydrogels

The mechanical robustness, self-healing capability, and anti-swelling behavior of the PNG hydrogels are synergistically governed by their hierarchical network architecture. To systematically evaluate these properties, we characterized hydrogels with varying AAc contents and gelatin fractions under different thermal conditions. As shown in Figure 4a, the tensile strength increased from 0.07 to 0.14 MPa with higher AAc loading, indicating enhanced structural integrity for biomedical support. As shown in Figure 4b, the optimal gelatin content was 15 wt%, beyond which the mechanical performance declined. Temperature-dependent mechanical tests revealed that, for a

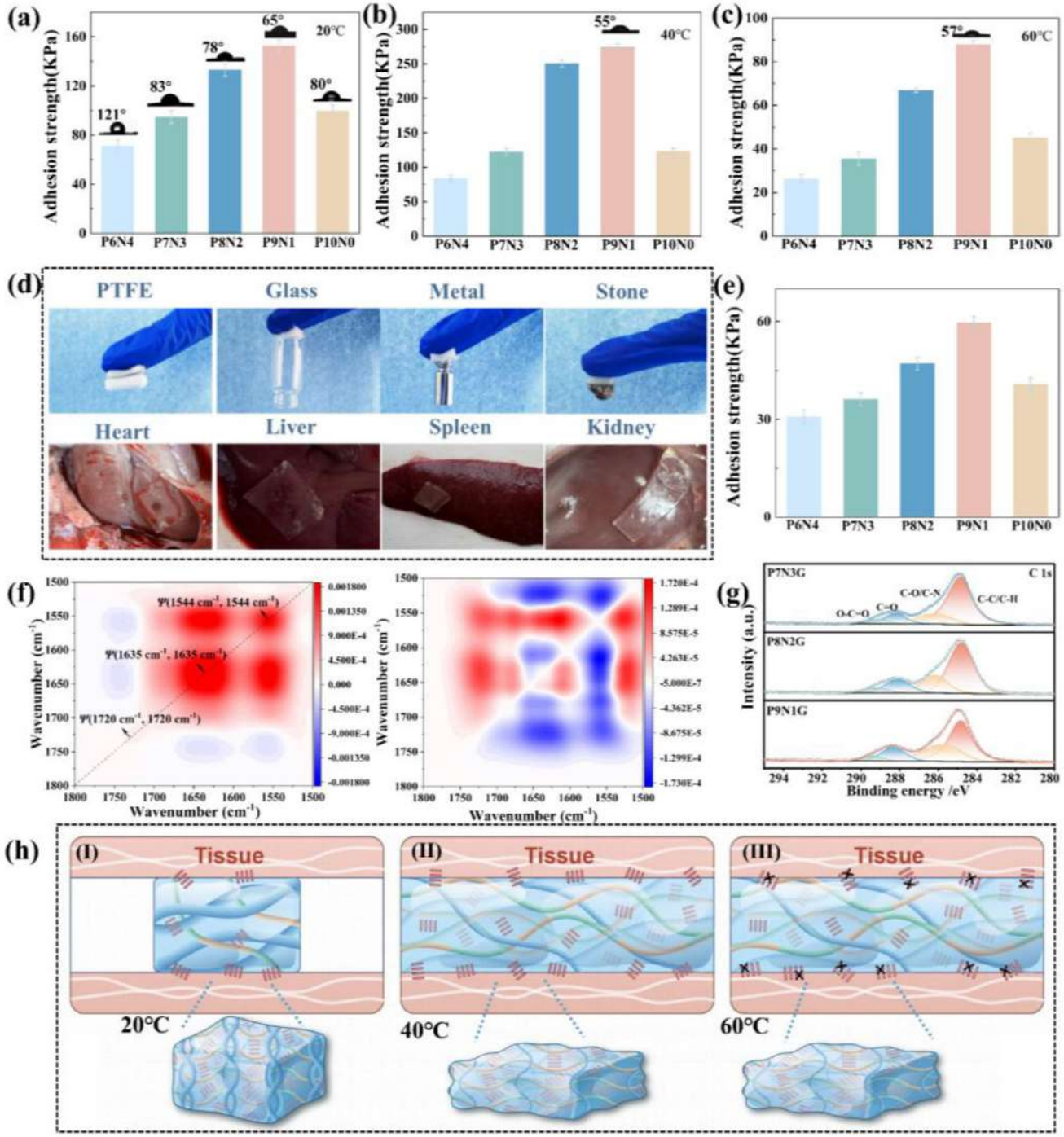

FIGURE 3 | Adhesive behavior of PNG hydrogel. a) Adhesion performance data and water contact angles of PNG hydrogels with different ratios at 20°C. b) Adhesion performance data of PNG hydrogels with different ratios at 40°C, along with the water contact angle of P9N1G. c) Adhesion performance data of PNG hydrogels with different ratios at 60°C, along with the water contact angle of P9N1G. d) Adhesion tests of the P9N1 hydrogel on multiple substrates and organs. e) Underwater adhesion data of the PNG hydrogel. f) 2D infrared spectroscopy data of the P9N1 PNG hydrogel: left: synchronous spectrum; right: asynchronous spectrum. g) XPS spectra of PNG hydrogels with different ratios. h) Schematic diagram of the adhesion mechanism of the PNG hydrogel.

representative PNG formulation, as the temperature increased from 0°C to 40°C, the tensile strength decreased from 0.26 to 0.1 MPa, while elongation at break increased from 528% to 770% showed in Figure 4c. This thermomechanical response corroborates the observed adhesion behavior, where higher stiffness facilitates intraoperative handling at lower temperatures, whereas enhanced ductility enables stronger adhesion at elevated temperatures.

The dynamic hydrogen-bond network confers remarkable self-healing capabilities. Figure 4d shows the self-healing properties of the PNG hydrogel. The P9N1 hydrogel was fabricated into

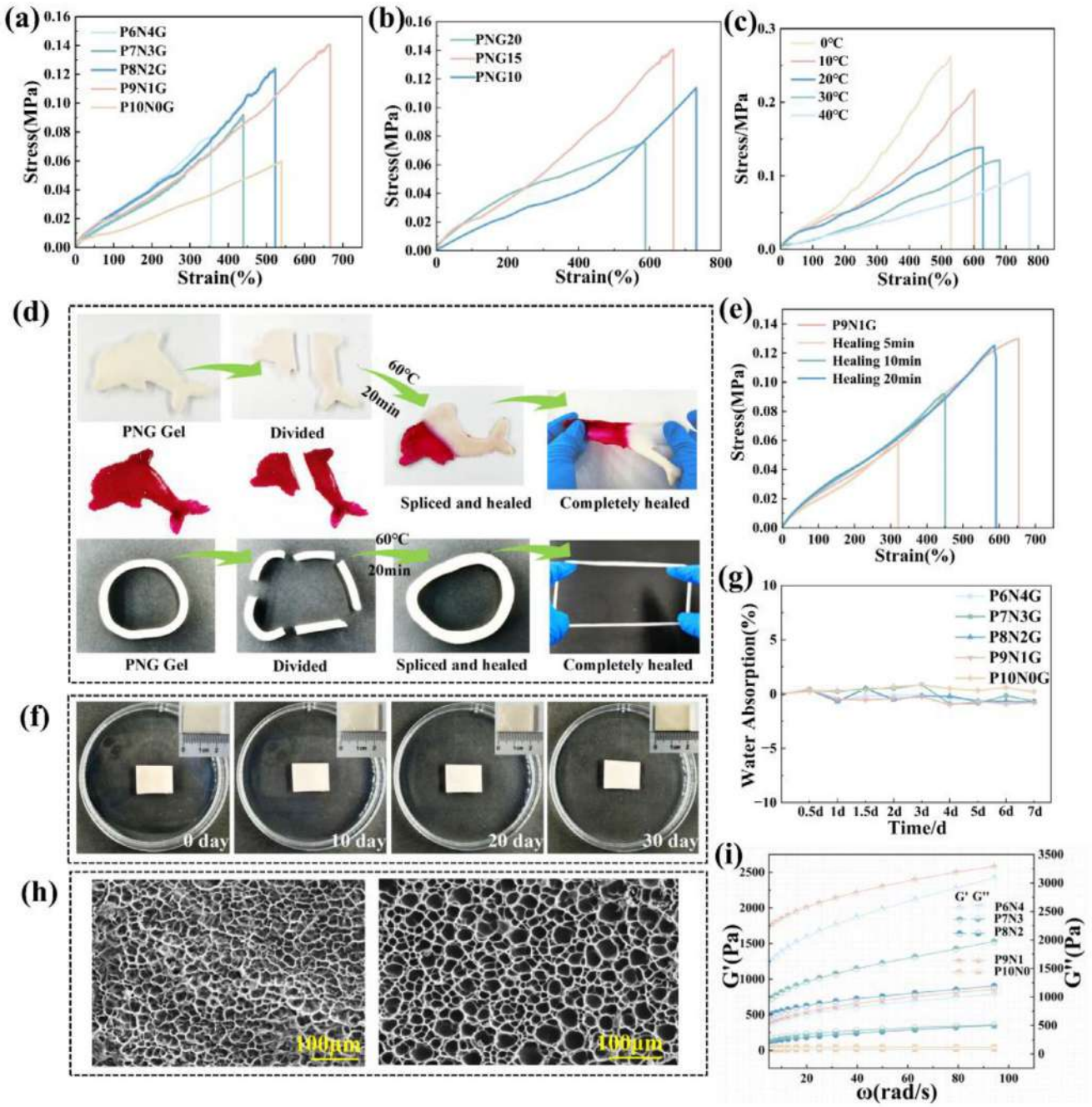

FIGURE 4 | a) Stress-strain curves of PNG hydrogels with different ratios at 20°C. b) Stress-strain curves of PNG hydrogels containing varying gelatin contents at 20°C. c) Stress-strain curves of the P9N1G hydrogel at different temperatures. d) Self-healing properties of the P9N1 hydrogel. e) Stress-strain curves of the P9N1G hydrogel after different healing times. f) Anti-swelling behavior of the PNG hydrogel. g) Anti-swelling curves of the PNG hydrogels with different ratios. h) Microstructure of the P9N1 hydrogel. i) Rheological test curves of the PNG hydrogel.

complex geometries (e.g., dolphin-shaped models) and patient-specific AF-like structures to demonstrate its superior processability, which were then severed and incubated at 60°C for 20 min. This treatment resulted in complete morphological restoration with a healing efficiency of 96% (Figure 4e). Furthermore, the P9N1 hydrogel can achieve self-healing at body temperature for 40 min. We tested the self-healing performance at different temperatures and found that the healing time decreases as the temperature increases showed in Figure S18. This adaptability suggests significant potential for the in situ repair of tissue defects and potentially reducing the risk of postoperative reherniation.

Crucially, for intervertebral disc applications, the hydrogel exhibits exceptional dimensional stability. The hydrogel maintained a near-zero swelling ratio over a 30-day observation period under physiological conditions and in a 7-day quantitative test in deionized water (Figure 4f,g), thereby minimizing the risk of nerve compression caused by material expansion. Furthermore, to simulate the physiological environment, an in vitro degradation assay was conducted in phosphate-buffered saline (PBS) at 37°C (Figure S19). The hydrogel exhibited a steady mass loss, reaching a degradation rate of approximately 41% over a 20-day period. This gradual breakdown profile is highly advantageous

for AF repair. During the critical early stage of tissue healing (the first 2–3 weeks), the hydrogel maintains sufficient mass and mechanical integrity to seal the AF defect and prevent nucleus pulposus reherniation. This remarkable anti-swelling performance stems from the formation of a dense cross-linked network between gelatin, AAc, and NAGA. Combined with the densely crosslinked framework previously established in Figure 2(i-iii), these features ensure outstanding structural stability in physiological environments, thereby reducing the risks associated with swelling-induced tissue compression.

The cross-sectional morphology of the PNG hydrogel was observed using an SEM. As depicted in Figure 4h, the P9N1 hydrogel exhibited a porous, dense network structure conducive to cell attachment while restricting water penetration. Notably, a decrease in pore size was observed with increasing AAc content, which is mainly due to the enhanced hydrogen bonding density. The viscoelastic properties shown in Figure 4i indicate that the storage modulus (G′) and loss modulus (G″) exhibit a non-monotonic trend with increasing AAc content. Initially, both G′ and G″ decrease as the AAc ratio increases from P7N3 to P8N2. This may be because the introduction of AAc gradually disrupts the original NAGA-dominated hydrogen bond clusters, thereby altering the interaction balance and slightly relaxing the network. However, when the AAc content increases to P9N1, the hydrogel's elasticity is significantly enhanced. This is attributed to the formation of a dense, highly coordinated hydrogen bond network driven by a large number of carboxyl groups at this ratio. Furthermore, these abundant carboxyl groups promote stronger electrostatic interactions between the polymer backbone and gelatin molecules, resulting in a higher modulus for the P9N1 hydrogel. Finally, when the system is converted to pure AAc (P10N0), the network relies solely on the inherent crosslinking of PAAc, leading to a significant decrease in the modulus.

Crucially, these comprehensive physical characterizations demonstrate the successful resolution of the adhesion-swelling paradox. Typically, highly crosslinked networks that resist swelling inherently restrict the polymer chain mobility required for tissue adhesion. However, our PNG hydrogel successfully breaks this trade-off. The dense AAc-NAGA hydrogen-bonded clusters provide exceptional structural integrity, while the thermally-actuated gelatin phase releases sufficient free chains at physiological temperature to achieve a robust adhesive strength. Considering its optimal balance of mechanical robustness, near-zero swelling, and superior thermo-responsive adhesion, the P7N3G, P8N2G, and P9N1G hydrogels were selected as the optimal candidate for all subsequent in vitro and in vivo biological evaluations.

2.5 | Cell Compatibility

The hydrogel exhibited a complex 3D network structure that closely mimicked the architecture of native extracellular matrix, thereby providing a highly favorable microenvironment for cell adhesion, spreading, and proliferation. Given these characteristics, assessing the cytocompatibility and biological activity of the hydrogel is crucial for determining its potential for use in tissue engineering and regenerative medicine. In the cell experiments described below, the Control group refers to cells cultured under standard conditions without any hydrogel treatment. Live/dead staining demonstrated that all the tested groups maintained high cell viability, with no significant cell death observed throughout the culture period (Figure 5a). This qualitative observation was further supported by quantitative analysis, which showed consistently low cytotoxicity across groups (Figure 5e). In addition, CCK-8 assays revealed a time-dependent increase in cell proliferation in all the groups, indicating that the hydrogels did not impede cell growth. The P9N1G hydrogel achieved the highest proliferation rate, suggesting superior cytocompatibility (Figure 5d).

Cytoskeletal staining provided additional insights into cell-material interactions. Cells cultured with the hydrogels exhibited enhanced spreading and well-organized actin filaments, particularly with the P9N1G hydrogel, indicating that its mechanical and biochemical properties better supported cytoskeletal remodeling and adhesion (Figure 5b). Furthermore, cell migration assays showed that the P9N1G hydrogel most effectively promoted directional migration and substrate attachment, as confirmed by quantitative analysis (Figure 5c,f).

Taken together, these findings demonstrate that the P9N1G hydrogel provides the most favorable biological environment among the tested formulations, exhibiting superior cytocompatibility and a strong capacity to promote cell adhesion, migration, and proliferation. These properties highlight the potential for future biomedical and regenerative applications.

2.6 | Extracellular Matrix Regeneration, Biosafety, and Tissue Adhesion

The expression levels of key AF repair-associated marker genes, including COL1, COL2, and ACAN, were assessed by quantitative real-time PCR (qRT-PCR) and western blot analysis to comprehensively evaluate the regenerative capacity of the hydrogels. The qRT-PCR results demonstrated a significant upregulation of all three markers in the P9N1G hydrogel, with expression levels markedly higher than those observed in the other groups (Figure 5g). This transcriptional enhancement suggests that the P9N1G hydrogel provides a more favorable microenvironment for extracellular matrix synthesis and AF tissue remodeling.

Western blotting further validated these findings at the protein level. Consistent with the gene expression data, the P9N1G hydrogel exhibited the strongest protein expression of COL1, COL2, and ACAN among all groups (Figure 5h). Notably, elevated levels of these matrix proteins indicate robust extracellular matrix deposition and structural reconstruction, both of which are essential for successful AF repair.

Taken together, the results of both gene and protein analyses provide compelling evidence that the P9N1G hydrogel most effectively stimulates AF matrix regeneration. Its ability to upregulate key anabolic markers highlights its superior potential to enhance AF healing, promote tissue remodeling, and restore disc structural integrity.

To assess the biocompatibility of the implanted hydrogels, the major organs of the experimental animals were histologically

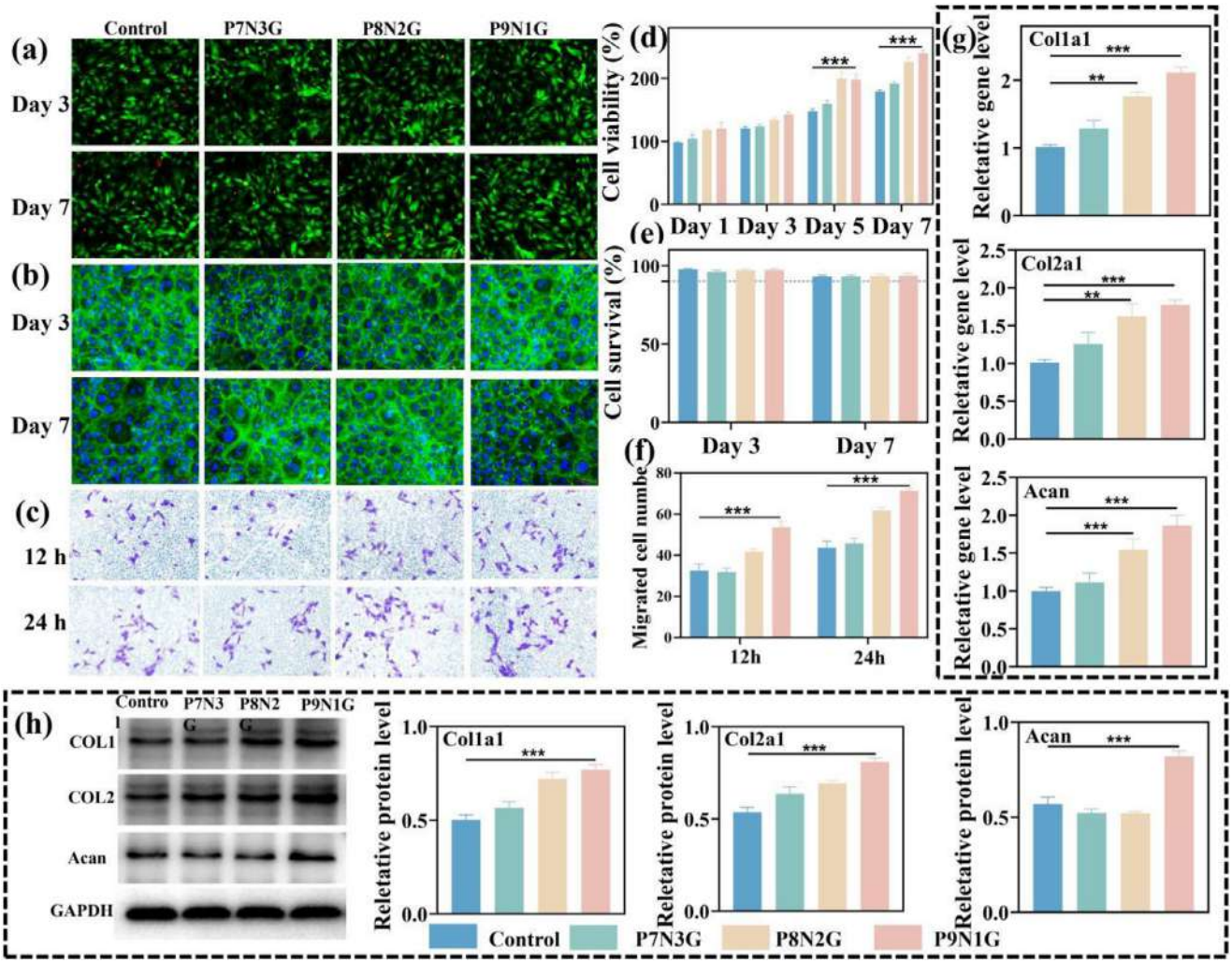

FIGURE 5 | Biocompatibility of the PNG hydrogel. a) Live/Dead staining. b) Cytoskeleton staining. c) Cell migration assay. d) CCK-8 assay. e)Quantitative analysis of cell viability. f)Quantitative analysis of cell migration. g) Gene expression of COL1, COL2, and ACAN. h) Protein expression of COL1, COL2, and ACAN. (*$p < 0.05$, **$p < 0.01$, ***$p < 0.001$, ****$p < 0.0001$).

examined. As shown in Figure S20, no abnormal inflammatory cell infiltration, tissue necrosis, edema, or other pathological alterations were observed in the heart, liver, spleen, or lungs of the rats. The normal histoarchitecture of these organs remained well preserved across all groups, indicating that hydrogel implantation did not induce systemic toxicity or adverse organ-specific responses. These findings further support the favorable biosafety profile of the hydrogel in vivo.

To further evaluate the hemostatic performance and adhesive capability of the hydrogel in vivo, additional experiments were conducted using various organs from rabbits and pigs. The results demonstrated that the hydrogel achieved effective hemostasis and strong adhesion across all the tested tissues, including the heart, liver, spleen, lungs, kidneys, and blood vessels. Following application, the hydrogel firmly adhered to the injured surfaces, and no recurrent bleeding or detachment of the hydrogel was observed during the observation period. These findings confirmed that the hydrogel provided reliable tissue adhesion and rapid hemostasis in multiple organ systems, highlighting its potential for broad clinical applications in soft tissue injury management (Figures S21 and S22).

2.7 | In Vivo Annulus Fibrosus Repair Assessment

Figure 6g illustrates the procedure used to establish the disc defect model and perform hydrogel implantation. A rat tail needle-puncture model was created to mimic AF injury. Under general anesthesia, the target intervertebral disc was surgically exposed by making a longitudinal skin incision of approximately 2 cm in length. An 18-gauge needle was used to puncture the AF to create a standardized defect. Subsequently, the hydrogel was carefully inserted into the defect site using fine forceps. After the layered closure of the muscle and skin, the implanted hydrogel remained well-positioned within the defect, indicating stable retention and successful model establishment. In Figure 6, the defect group, in which the annulus fibrosus was punctured but no hydrogel was implanted, served as the negative injury control. The normal/control group refers to intervertebral disc structures in a physiological state that have not undergone artificial disruption.

Radiographic evaluation was performed to assess changes in the intervertebral disc height and osteophyte formation in the rat caudal spine. In the defect group, the discs exhibited marked

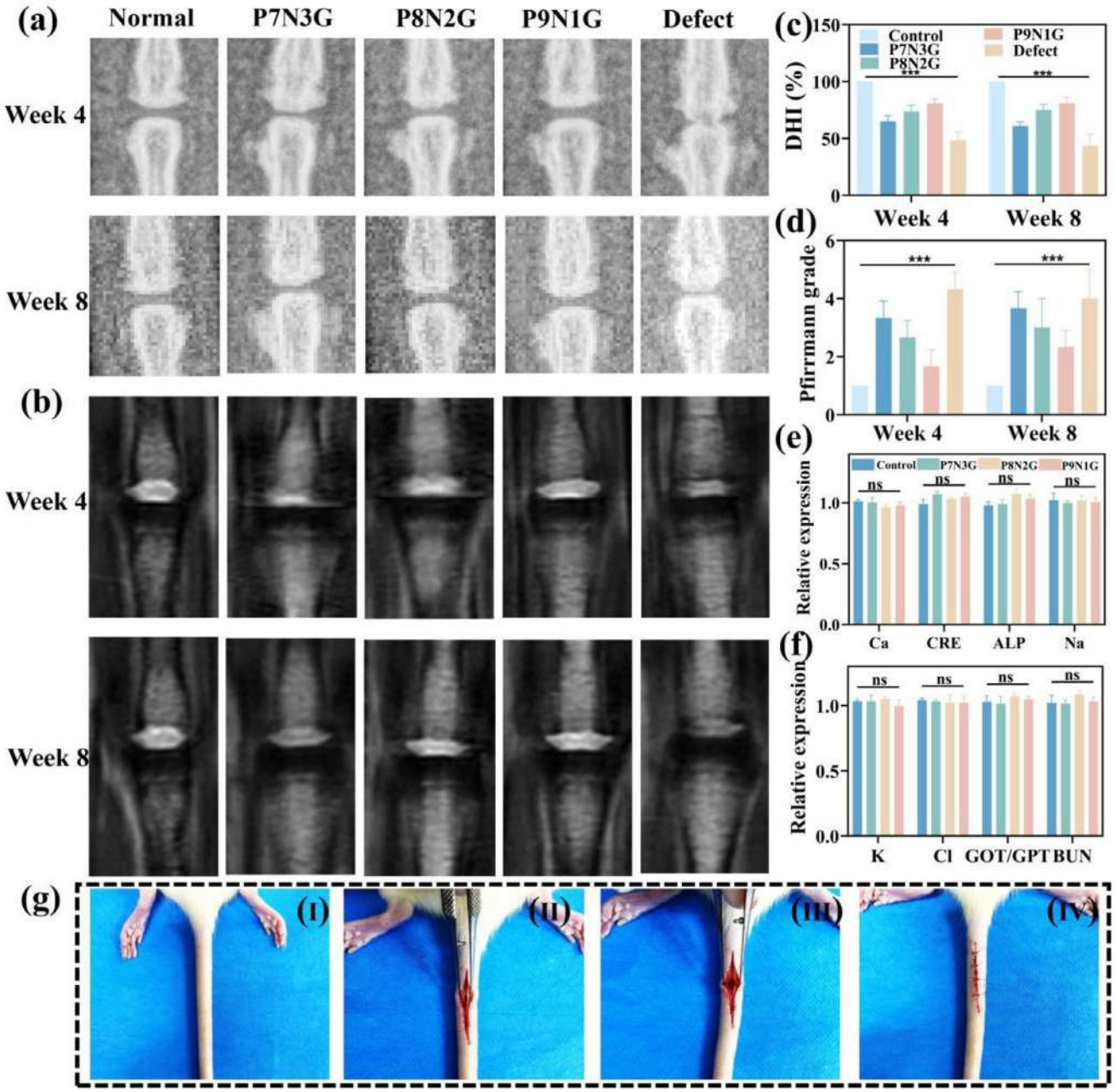

FIGURE 6 | a) X-ray images. b) MRI images. c) Quantitative analysis of disc height. d) Quantitative analysis of disc hydration status. e,f) Eight blood biochemical markers. g) Flowchart of the procedure for establishing the disc defect model and performing hydrogel implantation. (*$p < 0.05$, **$p < 0.01$, ***$p < 0.001$, ****$p < 0.0001$).

collapse accompanied by apparent damage to the adjacent vertebral endplates, indicating progressive structural deterioration. In contrast, among the hydrogel-treated groups, the P9N1G hydrogel demonstrated the greatest efficacy in maintaining the disc height, as clearly observed by X-ray imaging (Figure 6a). Quantitative analysis of the disc height further corroborated this trend, confirming the superior structural preservation provided by the P9N1G hydrogel (Figure 6c).

Subsequently, magnetic resonance imaging (MRI) assessment was conducted to evaluate disc hydration status and degeneration severity. Compared with the hydrogel-treated groups, the defect group showed substantial water loss from the intervertebral discs. Notably, the discs in the defect group exhibited pronounced hypointensity as early as 4 weeks postoperatively, indicating severe degeneration and dehydration. In contrast, the P9N1G hydrogel maintained a significantly higher relative water content at both 4 and 8 weeks, outperforming the other hydrogel formulations. This preservation of hydration was consistent with the modified Pfirrmann grading, in which the P9N1G hydrogel achieved more favorable scores, reflecting milder degenerative changes (Figure 6b,d).

Collectively, these radiographic and MRI findings demonstrate that the P9N1G hydrogel most effectively preserved disc height, maintained hydration, and slowed degeneration, underscoring

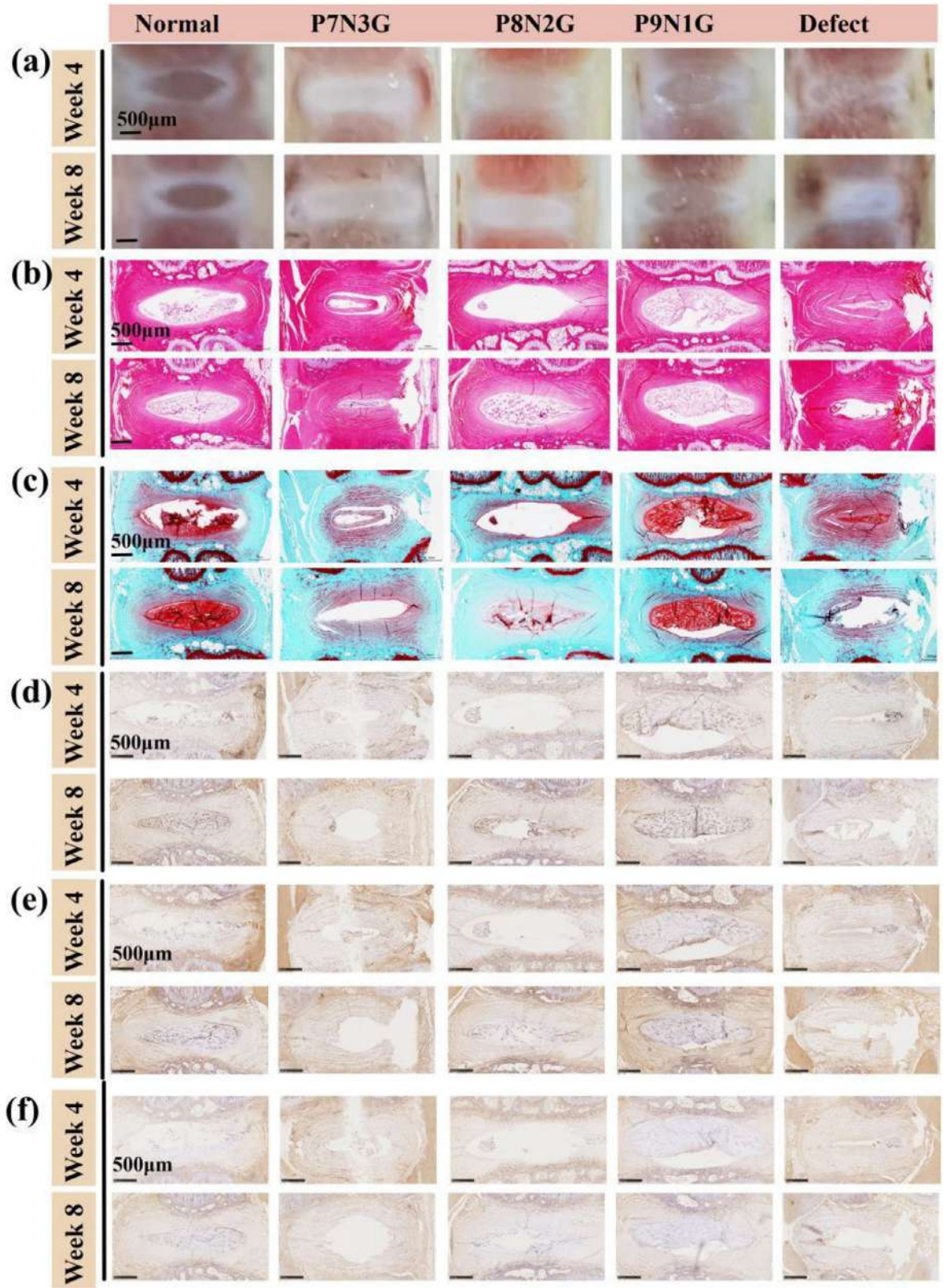

FIGURE 7 | a) Morphological images of the intervertebral disc. b,c) H&E and S&O histological staining. d) Immunohistochemical staining results for COL1. e) Immunohistochemical staining results for COL2. f) Immunohistochemical staining results for ACAN.

its strong therapeutic potential in promoting AF repair and mitigating intervertebral disc degeneration.

To evaluate the biological response following hydrogel implantation, eight blood biochemical markers and key serum ion concentrations were measured in rats. The results indicated that the implantation of the hydrogel did not induce any significant systemic effects, demonstrating good in vivo biosafety (Figure 6e,f).

To evaluate the in vivo therapeutic efficacy of the hydrogel in repairing the AF, we first examined the morphological changes within the intervertebral discs (Figure 7a). Macroscopic observations at 4 and 8 weeks postoperatively revealed substantial intergroup differences among the groups. Compared with the defect group, all hydrogel-treated groups exhibited markedly improved disc morphology, characterized by varying degrees of NP preservation and prevention of disc space collapse. Notably, in the P9N1G-treated group, the boundary between the AF and NP remained clearly distinguishable, whereas this boundary was blurred or difficult to identify in the P7N3G and P8N2G treated groups. A longitudinal comparison further demonstrated that the discs treated with the P9N1G hydrogel showed minimal morphological deterioration over time, in contrast to those treated with the P7N3G and P8N2G hydrogels, which exhibited evident NP shrinkage and structural compromise. This is due to the high elasticity of the P9N1 hydrogel. The significantly higher storage modulus of P9N1 provides mechanical support, thereby promoting cell spreading and proliferation. Furthermore, the construction of the polymer network plays a crucial role. The optimal AAc content in P9N1 provides abundant carboxyl groups, forming a dense network and generating stronger electrostatic and hydrogen bonding interactions with gelatin molecules. This effectively retains the gelatin containing the cell adhesion RGD motif within the scaffold, continuously providing a rich, cell-growth-friendly microenvironment, thus promoting stable cell adhesion and growth.

Histological analyses using hematoxylin and eosin (H&E) and safranin O-fast green (S&O) staining provided deeper insights into the repair process (Figure 7b,c). In the defect group, a pronounced defect gap persisted at both 4 and 8 weeks, accompanied by a near-complete loss of NP tissue. In contrast, the P9N1G hydrogel markedly reduced the defect gap at both time points, whereas the groups treated with the P7N3G and P8N2G hydrogels retained visible gaps with disorganized surrounding AF tissue. Moreover, notable cell infiltration was observed within the P9N1G hydrogel, with most infiltrating cells located at the interface between the hydrogel and adjacent native tissue. These cells exhibited a morphology consistent with that of AF cells, suggesting progressive tissue integration and remodeling following implantation.

Immunohistochemical staining further supported these observations (Figure 7d–f). Compared with the other groups, the P9N1G hydrogel group displayed the largest positive staining areas for COL1, COL2, and ACAN, indicating enhanced extracellular matrix synthesis and preservation of the disc structure. Together, these findings demonstrate that the P9N1G hydrogel not only effectively promotes AF defect repair but also delays disc degeneration by supporting tissue reconstruction and host-material integration.

3 | Conclusion

In summary, a double-network PNG hydrogel featuring an adhesion-swelling balance, superior cytocompatibility, and intrinsic self-healing capabilities was successfully engineered. The synergistic combination of MD simulations and experimental characterizations validated AAc as the optimal comonomer, elucidating the underlying mechanism of a pH-modulated hydrogen-bond crosslinking density threshold. Empowered by this dense yet dynamic hydrogen-bonded network, the hydrogel exhibits exceptional dimensional stability and robust mechanical properties in physiological environments, alongside a unique temperature-responsive adhesive behavior. In a rat AF defect model, the PNG hydrogel effectively mitigated intervertebral disc degeneration and facilitated the regeneration and functional reconstruction of the ECM. Collectively, these findings highlight the immense clinical translation potential of the PNG hydrogel in preventing post-discectomy reherniation and guiding tissue repair, thereby offering a novel functional biomaterial strategy for AF regeneration.

Acknowledgements

This work was supported by the Heilongjiang Provincial Natural Science Foundation of China (Grant 2022ZX02C25), National Natural Science Foundation of China (82372366) and Beijing Municipal Natural Science Foundation (L222096).

Conflicts of Interest

The authors declare no conflicts of interest.

Data Availability Statement

The data that support the findings of this study are available from the corresponding author upon reasonable request.

References

1. L. L. Fu, L. Li, Q. Y. Bian, et al., "Cartilage-Like protein hydrogels engineered via entanglement," *Nature* 618 (2023): 740–747, https://doi.org/10.1038/s41586-023-06037-0.

2. J. Xie, G. Huang, P. Wang, et al., "ROS-Scavenging Hydrogel Microneedles Reverse Intervertebral Disc Degeneration via Combined Mild Photothermal and NO Gas Therapy," *Advanced Functional Materials* 36 (2025): 792, https://doi.org/10.1002/adfm.202515474.

3. W. M. Han, S. J. Heo, T. P. Driscoll, et al., "Microstructural heterogeneity directs micromechanics and mechanobiology in native and engineered fibrocartilage," *Nature Materials* 15 (2016): 477–484, https://doi.org/10.1038/nmat4520.

4. Y. Ju, S. Ma, M. Fu, et al., "Polyphenol-modified biomimetic bioadhesives for the therapy of annulus fibrosus defect and nucleus pulposus degeneration After discectomy," *Acta Biomaterialia* 189 (2024): 116–129, https://doi.org/10.1016/j.actbio.2024.09.038.

5. L. Lu, Y. Li, W. Wang, et al., "A Biomimetic Silk Fibroin/Chitosan Membrane for Annulus Fibrosus Sealing to Prevent Intervertebral Disc Re-Herniation," *Advanced Healthcare Materials* 14 (2025): 202500228, https://doi.org/10.1002/adhm.202500228.

6. Y. Chen, C. Xue, F. Ni, et al., "Photothermal Hydrogel With Mn_3O_4 Nanoparticles Alleviates Intervertebral Disc Degeneration by Scavenging ROS and Regulating Extracellular Matrix Metabolism," *Advanced Functional Materials* 35 (2025): 49, https://doi.org/10.1002/adfm.202422817.

7. A. Samanta, T. Lufkin, and P. Kraus, "Intervertebral disc degeneration—Current therapeutic options and challenges," *Frontiers in Public Health* 11 (2023): 1156749, https://doi.org/10.3389/fpubh.2023.1156749.

8. H. W. Jiang, C. D. Chen, B. S. Zhan, Y. L. Wang, P. Tang, and X. S. Jiang, "Unilateral biportal endoscopic discectomy versus percutaneous endoscopic lumbar discectomy in the treatment of lumbar disc herniation: A retrospective study," *Journal of Orthopaedic Surgery and Research* 17 (2022): 30, https://doi.org/10.1186/s13018-022-02929-5.

9. F. Chen, L. Lei, S. Chen, et al., "Serglycin secreted by late-stage nucleus pulposus cells is a biomarker of intervertebral disc degeneration," *Nature Communications* 15 (2024): 47, https://doi.org/10.1038/s41467-023-44313-9.

10. Y. Wang, Y. Wu, B. Zhang, et al., "Repair of degenerative nucleus pulposus by polyphenol nanosphere-encapsulated hydrogel gene delivery system," *Biomaterials* 298 (2023): 122132, https://doi.org/10.1016/j.biomaterials.2023.122132.

11. Y. Chen, L. Zhang, X. Shi, et al., "Characterization of the Nucleus Pulposus Progenitor Cells via Spatial Transcriptomics," *Advanced Science* 11 (2024): 2303752, https://doi.org/10.1002/advs.202303752.

12. J. Li, Z. Ge, D. Zhang, et al., "Comparison of the efficacy of arthroscopic-assisted uni-portal spinal surgery and percutaneous endoscopic lumbar discectomy in the treatment of far lateral lumbar disc herniation: A retrospective controlled study," *European Spine Journal* 34 (2025): 4415–4427, https://doi.org/10.1007/s00586-025-08998-4.

13. M. C. Zhou, C. Yang, and Z. Nie, "Data fusion using Bayesian theory and reinforcement learning method," *Science China Information Sciences* 63 (2020): 170209, https://doi.org/10.1007/s11432-019-2751-4.

14. Q. Du, J. Li, F. Yang, H. Dai, and A. Wu, "Boundarics in Biomedicine," *Research* 7, no. 7 (2024): 0430, https://doi.org/10.34133/research.0430.

15. D. Zhou, W. Wang, W. Ma, et al., "Cartilage-Adaptive Hydrogels via the Synergy Strategy of Protein Templating and Mechanical Training," *Advanced Materials* 37 (2025): 2414081, https://doi.org/10.1002/adma.202414081.

16. T. Sun, Y. Liang, N. Ning, H. Wu, and M. Tian, "Strain-Insensitive Stretchable Conductive Fiber Based on Helical Core With Double-Network Hydrogel," *Advanced Fiber Materials* 7 (2025): 882–893, https://doi.org/10.1007/s42765-025-00530-z.

17. Q. Zhang, G. Kuang, L. Wang, P. Duan, W. Sun, and F. Ye, "Designing Bioorthogonal Reactions for Biomedical Applications," *Research* 6, no. 6 (2023): 0251, https://doi.org/10.34133/research.0251.

18. Y. Wang, P. Guan, R. Tan, X. Li, and J. Chen, "Fiber-Reinforced Silk Microneedle Patches for Improved Tissue Adhesion in Treating Diabetic Wound Infections," *Advanced Fiber Materials* 6 (2024): 1596–1615, https://doi.org/10.1007/s42765-024-00439-z.

19. M. Guo, H. Zhang, Y. Huang, et al., "Transcriptional Patterns of Nodal Entropy Abnormalities in Major Depressive Disorder Patients With and Without Suicidal Ideation," *Research* 8 (2025): 0659, https://doi.org/10.34133/research.0659.

20. S. Chen, W. Yao, Z. Ding, et al., "Injectable Electrospun Fiber-Hydrogel Composite Delivery System for Prolonged and Nociceptive-Selective Analgesia," *Advanced Fiber Materials* 6 (2024): 1428–1445, https://doi.org/10.1007/s42765-024-00422-8.

21. M. Gluais, J. Clouet, M. Fusellier, et al., "In vitro and in vivo evaluation of an electrospun-aligned microfibrous implant for Annulus fibrosus repair," *Biomaterials* 205 (2019): 81–93, https://doi.org/10.1016/j.biomaterials.2019.03.010.

22. X. Li, J. Gou, C. Maiti, and O. J. Ilegbusi, "Synthesis and characterization of ultra-soft alginate hydrogel mimicking lung tissue," *International Journal of Smart and Nano Materials* 15 (2024): 593–609, https://doi.org/10.1080/19475411.2024.2395261.

23. Y. Li, K. Zhang, X. Ai, et al., "A Biomimetic Peptide Functions as Specific Extracellular Matrix for Quiescence of Stem Cells Against Intervertebral Disc Degeneration," *Small* 19 (2023): 2300578, https://doi.org/10.1002/smll.202300578.

24. G. Jiang and W. Guo, "Research progress on conductive hydrogels derived From natural biopolymers as emerging interface materials for motion detection wearable sensors," *International Journal of Smart and Nano Materials* 16 (2025): 631–666, https://doi.org/10.1080/19475411.2025.2544149.

25. X. Li, Y. Liu, L. Li, et al., "Tissue-mimetic hybrid bioadhesives for intervertebral disc repair," *Materials Horizons* 10 (2023): 1705–1718, https://doi.org/10.1039/d2mh01242a.

26. W. Johannessen, J. M. Cloyd, G. D. O'Connell, E. J. Vresilovic, and D. M. Elliott, "Trans-Endplate Nucleotomy Increases Deformation and Creep Response in Axial Loading," *Annals of Biomedical Engineering* 34 (2006): 687–696, https://doi.org/10.1007/s10439-005-9070-8.

27. M. V. Risbud and I. M. Shapiro, "Role of cytokines in intervertebral disc degeneration: Pain and disc content," *Nature Reviews Rheumatology* 10 (2014): 44–56, https://doi.org/10.1038/nrrheum.2013.160.

28. G. M. Taboada, K. Yang, M. J. N. Pereira, et al., "Overcoming the translational barriers of tissue adhesives," *Nature Reviews Materials* 5 (2020): 310–329, https://doi.org/10.1038/s41578-019-0171-7.

29. M. Liu, Z. Cui, D. Xu, C. Liu, and C. Zhou, "Chitin nanocrystal-reinforced chitin/collagen composite hydrogels for annulus fibrosus repair After discectomy," *Materials Today Bio* 31 (2025): 101537, https://doi.org/10.1016/j.mtbio.2025.101537.

30. B. Gong, J. Lin, Y. Xie, and J. Qian, "A combined numerical and theoretical study on the strengthening and toughening mechanisms of double network hydrogels," *International Journal of Smart and Nano Materials* 16 (2025): 284–308, https://doi.org/10.1080/19475411.2025.2476130.

31. Y. Shen, L. Pang, C. Jiang, et al., "Extracellular Vesicles Functional "Brick-Cement" Bio-Integrated System for Annulus Fibrosus Repair," *Advanced Functional Materials* 34 (2024): 2400066, https://doi.org/10.1002/adfm.202400066.

32. F. Usta, F. Scarpa, H. S. Türkmen, P. Johnson, A. W. Perriman, and Y. Chen, "Multiphase lattice metamaterials With enhanced mechanical performance," *Smart Materials and Structures* 30 (2021): 025014, https://doi.org/10.1088/1361-665X/abd15d.

33. J. Yang, T. Yu, J. Yao, et al., "Improving flexible actuating behaviors of gel-based artificial muscles Through chamomile polysaccharide crosslinking," *Smart Materials and Structures* 33: 125045, https://doi.org/10.1088/1361-665X/ad8f7e.

34. B. Zhu, Y. Cai, L. Zhou, et al., "Injectable supramolecular hydrogel co-loading abemaciclib/NLG919 for neoadjuvant immunotherapy of triple-negative breast cancer," *Nature Communications* 16 (2025): 687, https://doi.org/10.1038/s41467-025-55904-z.

35. M. Yang, C. Yuan, X. Chen, X. Jiang, and T. Wang, "Prototyping sutureless shape memory valve stent via integrated 3D printing," *Smart Materials and Structures* 34: 015003, https://doi.org/10.1088/1361-665X/ad939f.

36. K. Zhang, Y. Wei, H. Ding, et al., "Modular Design of Hydrogel Adhesives for Enhanced Tissue Healing," *Advanced Materials* 38 (2026): 16770, https://doi.org/10.1002/adma.202516770.

37. X. Li, X. Li, J. Hu, et al., "Spheroid-Derived BMSC Exosomes Enhance Proliferation and Matrix Remodeling of Nucleus Pulposus Cell Clusters in Degenerative Disc Repair," *Small* 21 (2025): 07073, https://doi.org/10.1002/smll.202507073.

38. M. L. Tian, J. J. Wan, X. Wang, et al., "Anisotropic nanocomposite hydrogel dressings With thermo-responsive contraction for actively stimulated tissue regeneration," *Chemical Engineering Journal* 514 (2025): 163202, https://doi.org/10.1016/j.cej.2025.163202.

39. L. Huang, W. Wang, Y. Xian, et al., "Rapidly in situ forming an injectable Chitosan/PEG hydrogel for intervertebral disc repair," *Materials Today Bio* 22 (2023): 100752, https://doi.org/10.1016/j.mtbio.2023.100752.

40. M. Zhang, W. T. Hao, Z. Fu, Y. Huang, F. H. Yan, and D. L. Ni, "Self-assembled magnesium peroxide supramolecular hydrogel for oxidants neutralization and chemical burn management," *Bioactive Materials* 57 (2025): 154–168, https://doi.org/10.1016/j.bioactmat.2025.11.002.

41. J. Deng, H. Yuk, J. Wu, et al., "Electrical bioadhesive interface for bioelectronics," *Nature Materials* 20 (2021): 229–236, https://doi.org/10.1038/s41563-020-00814-2.

42. Y. N. Mai, H. L. Wang, J. Y. Lu, et al., "Catalyst-modulated hydrogel dynamics for decoupling viscoelasticity and directing macrophage fate for diabetic wound healing," *Bioactive Materials* 52 (2025): 878–895, https://doi.org/10.1016/j.bioactmat.2025.06.007.

Supporting Information

Additional supporting information can be found online in the Supporting Information section.

Supporting File: smll74894-sup-0001-SuppMat.docx.